Accepted Manuscript

Surfactant-free solvothermal synthesis of Hydroxyapatite nested bundles for the effective photodegradation of cationic dyes

I. Reeta Mary, S. Sonia, D. Navadeepthy, D. Mangalaraj, C. Viswanathan, N. Ponpandian
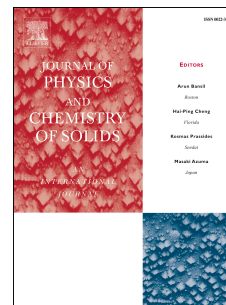
Please cite this article as: I.R. Mary, S. Sonia, D. Navadeepthy, D. Mangalaraj, C. Viswanathan, N. Ponpandian, Surfactant-free solvothermal synthesis of Hydroxyapatite nested bundles for the effective photodegradation of cationic dyes, *Journal of Physics and Chemistry of Solids* (2018), doi: 10.1016/ j.jpcs.2018.01.035.

Graphical Abstract

Surfactant-Free Solvothermal Synthesis of Hydroxyapatite Nested Bundles for the Effective Photodegradation of Cationic Dyes

I. Reeta Mary,[a,b] S. Sonia,[a] D. Navadeepthy,[a] D. Mangalaraj,[a] C. Viswanathan,[a] and N. Ponpandian[a,*]

[a]Department of Nanoscience and Technology, Bharathiar University, Coimbatore 641046, India

[b]Department of Physics, Government Arts College, Coimbatore 641018, India

*Corresponding author: ponpandian@buc.edu.in (N. Ponpandian)

Abstract

In this study, hydroxyapatite nested bundles (HNBs) were successfully constructed from nanosticks as nanoscale building blocks via a facile, solvothermal process without using any surfactant. The fabricated HNBs were structurally analyzed using X-ray diffraction and Fourier transform infrared spectroscopy, which confirmed the purity of the HNBs. The surface characteristics were determined by field emission scanning electron microscopy and Brunauer–Emmett–Teller analysis, and the optical characteristics by ultraviolet (UV)-visible spectroscopy. The synthesized HNBs were tested to determine their activity during the degradation of methylene blue, methylene violet, and rhodamine B via photocatalysis under UV irradiation. The degradation efficiency of HNBs and the rate of degradation can be explained based on the properties of the HNBs and cationic dyes.

Keywords: cationic, degradation, nested bundle, photocatalysis

1. Introduction

Modern technology has been progressing towards greater control over the structure of matter for millennia in order to reduce the dimensions of devices and active materials. Despite these developments in various fields, maintaining a clean environment is a major problem that humanity has faced in recent years. Water pollution is among the most important environmental issues, where it is often caused by industrial effluents containing dyes from the textile, paper, leather, dying, printing, and other industries [1]. The generation of large quantities of organic pollutants and toxic substances by these industries causes environmental problems, as well as lead to health issues that affect entire ecosystems. The presence of even a small amount of dye in wastewater can severely affect aquatic life [2,3] because dyes have carcinogenic, mutagenic, and allergenic properties [4]. Cationic dyes are more toxic than anionic dyes because of their synthetic origins and due to the presence of an aromatic ring structure with delocalized electrons

1

[5]. Most dyeing industries prefer cationic dyes because they are readily soluble in water and easier to apply to fabrics [6]. Hence, the removal of cationic dyes such as methylene blue (MB), methylene violet (MV), and rhodamine B (RhB) from wastewater is an environmental challenge due to their severe health effects on living organisms [7-9].

The application of nanometer-scale objects is considered as a possible solution to various ecological problems [10]. The vast increase in the specific surface area of nanomaterials obtained by scaling down to the nanoscale enhances their physical and chemical properties [11]. These properties usually depend on the size, morphology, specific surface area, pore size, surface roughness, *etc.*, of the nanoscale materials, and they have various applications in environmental remediation. Thus, contaminated water can be treated with nanostructured materials that degrade organic dyes in an efficient manner. Hence, the production of biocompatible nanostructured materials with desirable morphologies using suitable eco-friendly methods for environmental applications is a great challenge. Among the various methods for synthesizing nanostructures, such as sol–gel, co-precipitation, reflux condensation, electrodeposition, and microemulsion approaches, the hydro/solvothermal method is an inexpensive and controllable method for directing structures under mild synthetic conditions [12-16].

Nanostructured hydroxyapatite (HAp) is a well-known biocompatible material, which has a wide range of applications such as catalysis, adsorption, sensing, retarding cancer cell growth, and drug delivery. In particular, HAp selectively adsorbs various ions, organic compounds, and proteins, which make it an appropriate material for water treatment [17]. For instance, the photocatalytic behavior of HAp with methyl mercaptane has been studied and its photocatalytic decomposition due to the formation of radical species under ultraviolet (UV) irradiation [18] was explained. The degradation of MB (62%) by HAp in oxygen saturated water was also reported [19] and the photocatalytic activity with dimethyl sulfide based on the crystallinity of HAp [20] was investigated. However, studies of the effectiveness of photocatalysis using HAp nested bundle (HNB) microstructures with cationic dyes such as MV and RhB have not been reported previously.

Thus, in this study, we conducted the surfactant-free synthesis of HNBs from nanosticks as nanoscale building blocks via a solvothermal process. The structural, surface, and optical properties of the HNBs were characterized using appropriate techniques. We conducted

systematic investigations of the photocatalytic degradation of MB, MV, and RhB using the HNBs under UV irradiation, and determined the effective degradation efficiency.

2. Experimental section

2.1. Materials

Calcium nitrate tetrahydrate ($Ca(NO_3)_2.4H_2O$), diammonium hydrogen phosphate (($NH_4)_2HPO_4$), 30% ammonia solution (NH_4OH), ethanol (EtOH; C_2H_5OH), MB ($C_{16}H_{18}ClN_3S$), MV ($C_{14}H_{12}N_2OS$), and RhB ($C_{28}H_{31}ClN_2O_3$) were obtained from SDFCL, India. All of the chemicals were analytical grade and they were used as received.

2.2. Surfactant-free synthesis of HNBs

Nanostructured HNBs were produced via a solvothermal process without using any surfactant. In the typical route used for producing HNBs, 0.3 M diammonium hydrogen phosphate was dissolved in 20 mL of distilled water (DW), before adding 10 mL of EtOH slowly, and the pH of the phosphate solution was then adjusted to 10 using aqueous ammonia. This phosphate solution was then added in a dropwise manner to 0.5 M calcium nitrate tetrahydrate solution with DW and EtOH in the same ratio of 1:0.5. This mixture was transferred to a 75 mL Teflon-lined autoclave, which was sealed and heated at 180°C for 12 h in a hot air oven. The final precipitate was washed several times with DW and dried in an oven at 100°C before further characterization.

The reactions were conducted by varying the ratio of DW relative to EtOH among 1:0, 1:0.2, and 1:0.5. The optimized nanostructured HNBs were obtained using a ratio of 1:0.5. The prepared HNBs were subjected to further characterization.

2.3. Characterization of HNBs

Structural analysis of the HNBs was performed by X-ray diffraction (XRD) using a PANalytical X'Pert Pro X-ray diffractometer with monochromatic high intensity Cu $K\alpha_1$ radiation (λ = 1.5406 Å) and a Brucker Tensor 27 Fourier transform infrared (FTIR) spectrometer. The surface morphology was analyzed by field emission scanning electron microscopy (FESEM) using an FEI Quanta-250 FEG field emission scanning electron microscope. Samples were gold sputtered at a low deposition rate before morphological examination. The surface characteristics were determined by generating nitrogen adsorption–desorption isotherms using an Autosorb-1 system (Quantachrome Instruments). The samples were outgassed at 110°C under 10^{-2} mm Hg for more than 6 h before obtaining the measurements. The pore size and pore volume of the samples were obtained according to the Barrett–Joyner–Halenda method, and the surface area was measured

3

with the Brunauer–Emmett–Teller (BET) method [21] by utilizing the nitrogen adsorption/desorption procedure. Optical studies and photocatalytic absorption measurements were performed using a JASCO UV-visible (Vis) spectrophotometer.

2.4. Photocatalytic studies

The photocatalytic activities of the HNBs were evaluated at room temperature using MB, MV, and RhB as model cationic pollutants, which are abundant in industrial effluents. In a typical procedure, 0.025 g of the photocatalyst was dispersed in 50 mL of a 2 ppm aqueous solution of MB. The solution was stirred in the dark to establish an adsorption/desorption equilibrium between the photocatalyst and the dye molecules. The solution was then illuminated by a UV source (λ_{max} = 365 nm) to induce a photochemical reaction. Samples were collected at regular intervals and centrifuged to separate any particles before their analysis. The same procedure was repeated for the MV and RhB dye solutions. The concentration of the pollutant in the solution during the photocatalytic degradation reaction was monitored by measuring the absorbance using an UV-Vis spectrophotometer.

3. Results and Discussion

3.1. Structural analysis of HNBs

The structure and phase composition of the HNBs were investigated by powder XRD. The average crystallite size and lattice parameters were also calculated using appropriate formulae. The XRD patterns obtained for the reaction series during the synthesis of HNBs are shown in Fig. 1. The diffraction peaks were readily indexed to the standard JCPDS (#73-0293) for HAp. The peaks at 25.39°, 28.66°, 31.56°, 32.76°, 33.80°, 39.43°, 46.44°, 49.16°, 52.91°, 63.68°, and 77.52° corresponding to the (002), (210), (211), (300), (202), (212), (401), (213), (004), (304), and (513) planes, respectively, indicated the crystallinity and hexagonal structure of the phase pure HNBs. The absence of impurity peaks or intermediate/secondary phase compounds also demonstrated the purity of the samples [22]. The lattice constants for the hexagonal HNBs were $a = b$ = 9.4824 Å and c = 6.8927 Å, and the average grain size was calculated as 21 nm.
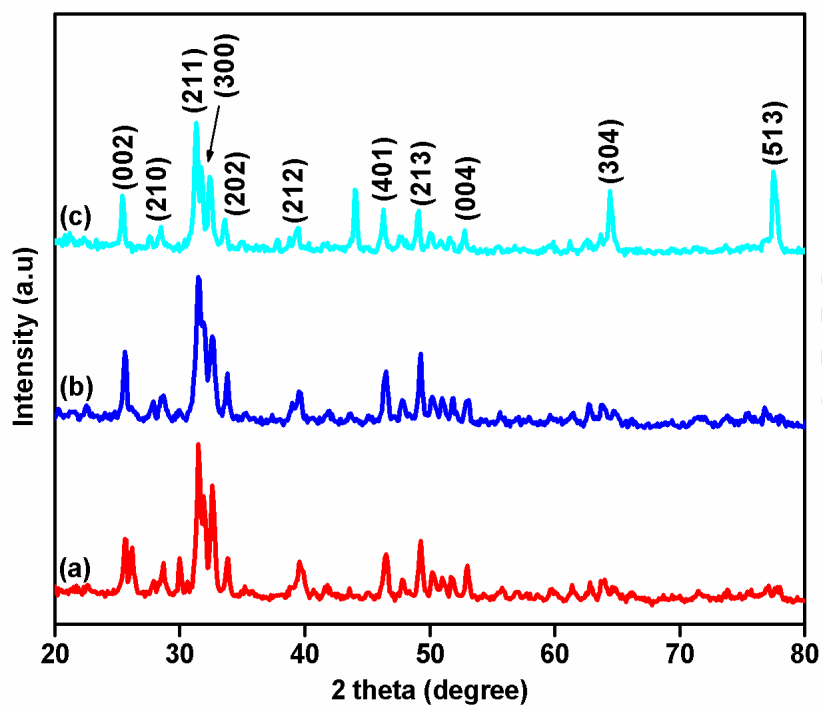
Fig. 1 XRD patterns obtained for HNBs prepared by varying the DW to EtOH ratio among: (a) 1:0, (b) 1:0.2, and (c) 1:0.5.
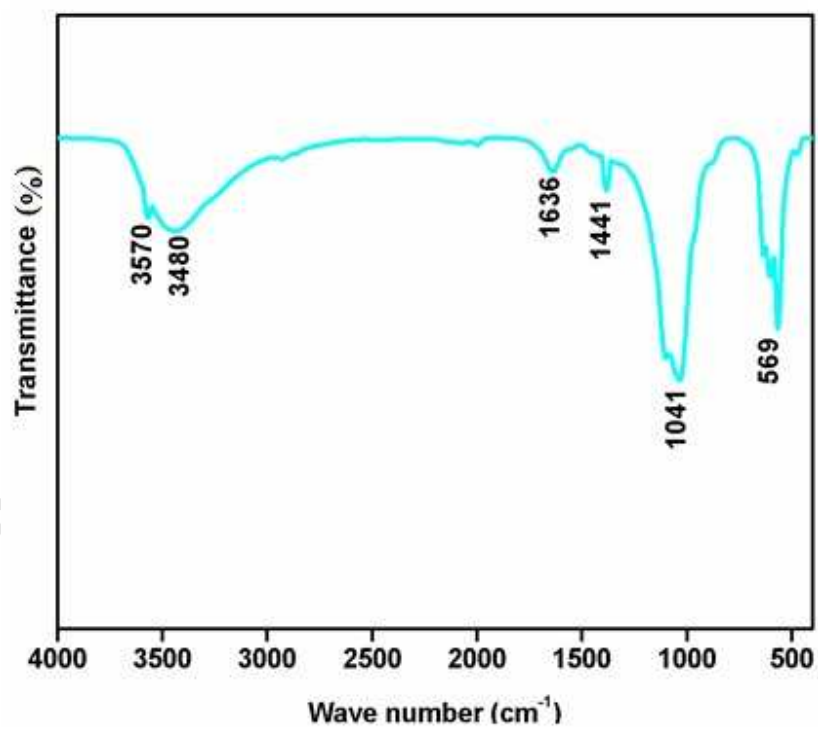

Fig. 2. FTIR spectrum obtained for HNBs.

5

The molecular structure and bonding nature of the HNBs was validated by FTIR analysis in the wavenumber range of 400–4000 cm^{-1}, and the spectrum is shown in Fig. 2. Theoretically, the ν_1 and ν_3 phosphate bands, and ν_4 absorption bands observed in the regions of 900–1200 cm^{-1} and 500–700 cm^{-1}, respectively, characterized the apatite structure [23]. Intense peaks attributed to PO_4^{3-} stretching and bending modes at 1041 and 569 cm^{-1}, respectively, confirmed the apatite structure. The peak at 1441 cm^{-1} may be attributable to carbonate ions originating from atmospheric carbon dioxide during sample preparation [24]. The broad band at 3480 cm^{-1} could be assigned to the water adsorbed on HNBs and the transmittance peak at 1636 cm^{-1} was attributed to the bending mode of H_2O. The shoulder peaks at 630 and 3570 cm^{-1} were the characteristic vibrational stretching and bending modes, respectively, of stoichiometric HAp [25]. The FTIR spectra also showed that no impurity peaks were present due to additives or other non-stoichiometric apatites, thereby demonstrating the purity of the prepared HNBs.

3.2. Surface analysis of HNBs

The surface investigation of nanostructured materials has a key role in determining the structural, optical, and surface properties of materials, which can be applied in various fields. The surface profile and adsorption characteristics of the HNBs were determined by FESEM and BET analyses.
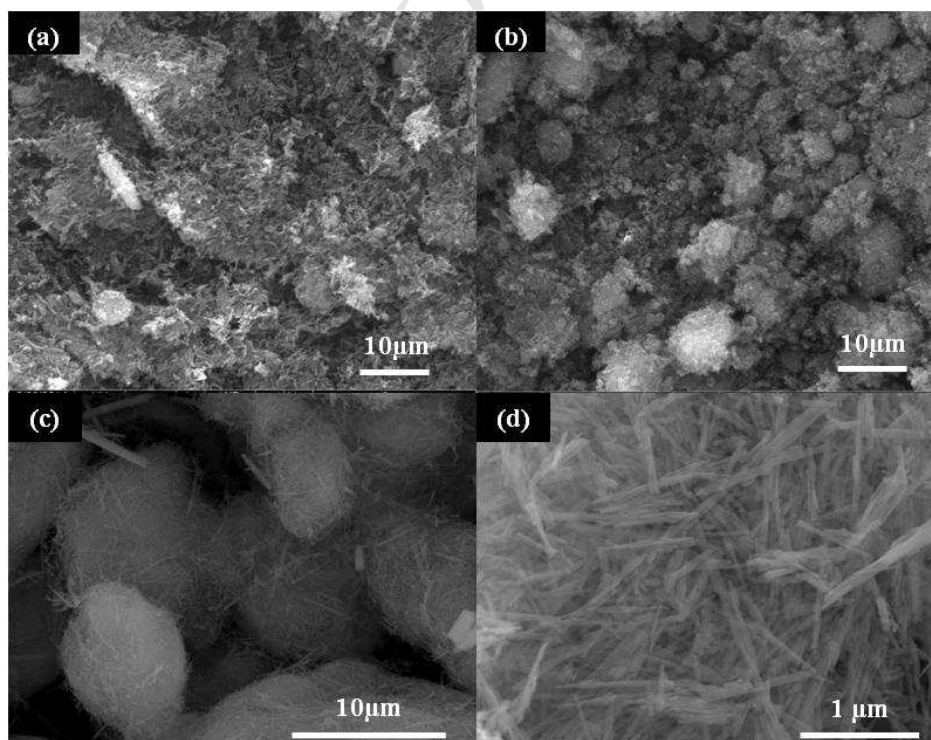
Fig. 3 FESEM images of HABs prepared by varying the DW to EtOH ratio among: (a)1:0, (b) 1:0.2, and (c) 1:0.5; and (d) high magnification image with a ratio of 1:0.5.

The formation of nested bundles was observed in the FESEM images, as shown in Fig. 3. Series of reactions were conducted by varying the amount of EtOH in the DW–EtOH solvent system. The formation of HAp nanorods was observed due to initial nucleation and growth processes when the solvent was DW alone, as shown in Fig. 3(a). When EtOH was introduced into the reaction medium, the clusters of nanorods tended to form a nest-like structure (see Fig. 3(b)). The dielectric constant and viscosity of solvents influence nucleation as well as the preferential direction of crystal growth [26-28]. The higher dielectric constant and lower viscosity of the DW favored the growth of nanorods into nanosticks, whereas the lower dielectric constant and higher viscosity of EtOH were responsible for the overall architecture of the HNBs constructed via the self-assembly of nanosticks as nanoscale building blocks in the double solvent system [29]. Figures 3(c) and 3(d) show the HNBs and their nanoscale building blocks, respectively. The formation of well-dispersed nested bundles is clearly visible in the images, with an average length and width of 11 and 5 µm, respectively, and with a typical aspect ratio of 2.2. The average dimensions of the nanosticks were 1.5 µm by 20 nm. The nanosticks formed during nucleation acted as building blocks that self-assembled to form nested bundles with a unique microstructure. The EtOH mixed as a solvent with DW to act as a stabilizing agent that influenced the growth kinetics of the HNBs.
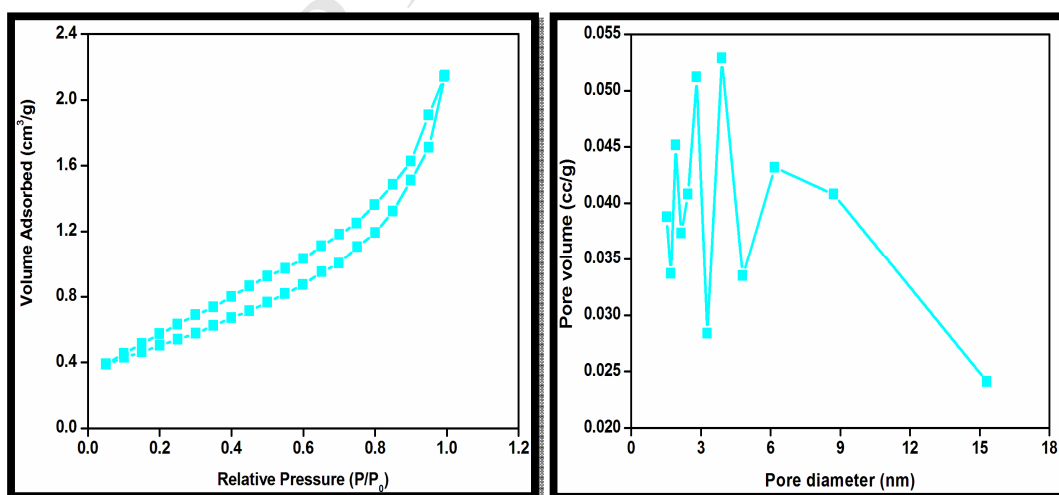

Fig. 4 Nitrogen adsorption–desorption isotherm and pore size distribution of HNBs.

The nitrogen adsorption–desorption isotherms and the pore size distributions of the HNBs determined by BET analysis are shown in Fig. 4. The isotherms were characterized by a distinct hysteresis loop in the region of 0.04 to 1 P/P_0. According to the International Union of Pure and Applied Chemistry (IUPAC), the fabricated nanostructured surfaces were predominantly mesoporous based on the type IV isotherms [30]. The shape of the hysteresis loop exhibited by the HNBs was type H3, which confirmed the mesoporous structure of the HNBs derived from particle aggregates with slit-shaped pores [31-33]. The calculated specific surface area and pore size were 31.09 m^2 g^{-1} and 15 nm, respectively.

3.3. Optical analysis of HNBs

The synthesized HNBs were subjected to optical studies by UV-Vis spectrophotometry. The absorption spectrum and the Kubelka–Munk plot obtained for the HNBs are shown in Fig. 5. The absorption edge wavelength was observed at 257 nm. The optical band gap can be obtained by plotting *hv* versus $(\alpha h v)^2$ in the high absorption range, before extrapolating the linear portion of the absorption edge to find the intercept with the X-axis (energy). The optical band gap estimated for the HNBs was 5.1 eV, which is similar to that reported in a previous study [34].
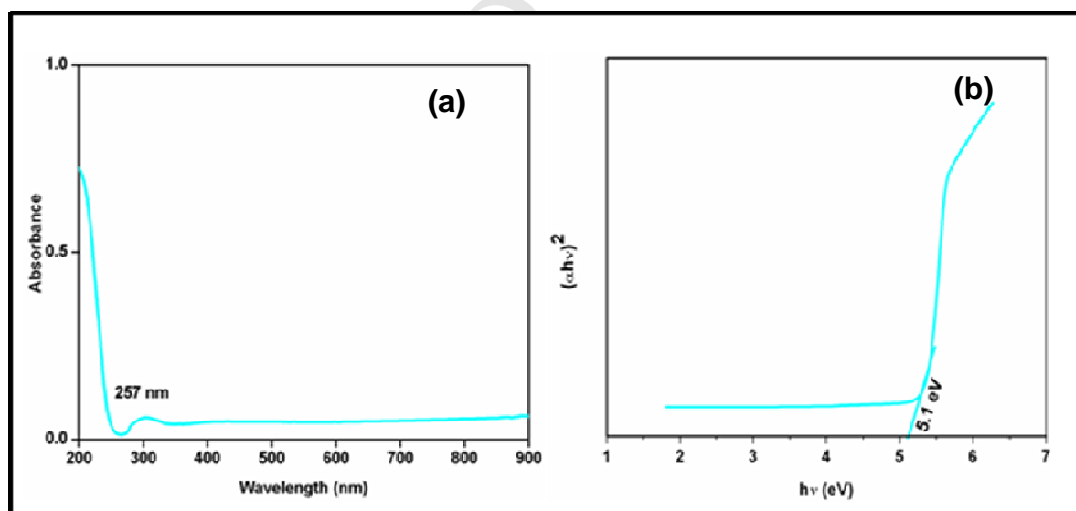

Fig. 5 (a) UV-Vis absorption spectrum and (b) Kubelka–Munk plot of the band gap determined for HNBs.

3.4. Photocatalytic activity of HNBs

3.4.1. Photocatalytic studies

HAp exhibits the selective adsorption of various organic compounds [35] where its structural, surface, and optical properties significantly influence its photocatalytic activity. Photodegradation experiments were conducted using cationic dye solutions of MB, MV, and RhB with and without HNBs (photocatalyst) under an UV irradiation source at room temperature.

The degradation efficiency of the HNBs was calculated using the formula:

$$\eta\% = (1 - A/A_0) \times 100$$,

where A_o is the absorption maximum at t = 0 and A is the absorption maximum at time t = t min. The photocatalytic degradation of the organic dyes by the nanostructures under UV light followed pseudo-first order kinetics with respect to the absorption intensity of the dyes, as follows:

$$-\frac{dA}{dt} = K_{app}A$$,

where integration yields:

$$-ln(A/A_0) = K_{app}t$$

where K_{app} and t are the apparent reaction rate constant and irradiation time, respectively. Thus, the plot of t versus $-ln\ (A/A_o)$ yields the slope of K_{app}, which is the degradation rate constant.
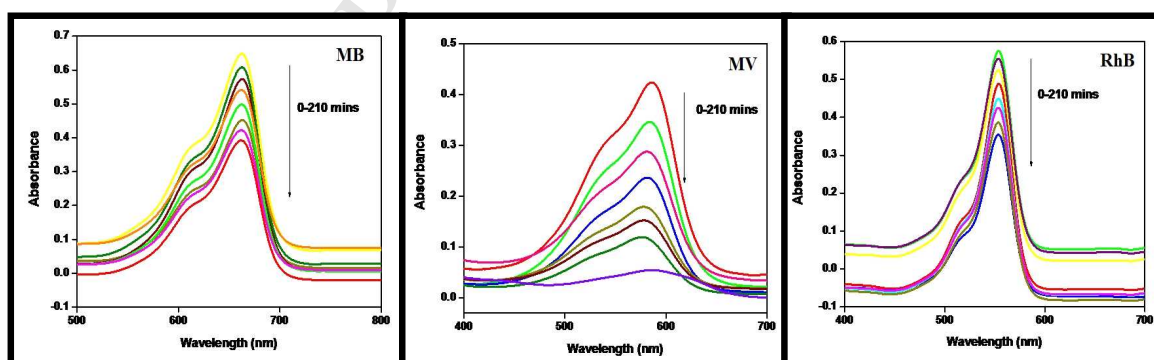

Fig. 6 Photodegradation absorption spectra obtained for MB, MV, and RhB with HNBs.

The absorption spectra obtained for MB, MV, and RhB as well as their concentrations in solution after centrifugation when sampled at regular intervals of 30 min are presented in Fig. 6. Clearly, the absorption peaks of all the dyes decreased gradually as the exposure time increased from 0 to 210 min, thereby demonstrating the ability of the HNBs to effectively degrade various cationic dyes.

The degradation efficiencies and the degradation rate constants of the HNBs with the MB, MV, and RhB dyes are shown in Fig. 7. The linearity of the plot of t versus $-ln(A/A_o)$ suggests that the photodegradation reaction between the HNBs and the dyes followed pseudo-first order kinetics. In addition, the degradation rate of MV was higher compared with those of MB and RhB. The degradation efficiency of MB and RhB reached 77–81% after UV irradiation for 210 min, whereas that of MV reached 91% after the same period of time. The degradation efficiencies and the degradation rate constants calculated for the HNBs with MB, MV, and RhB using appropriate formulae are given in Table 1.
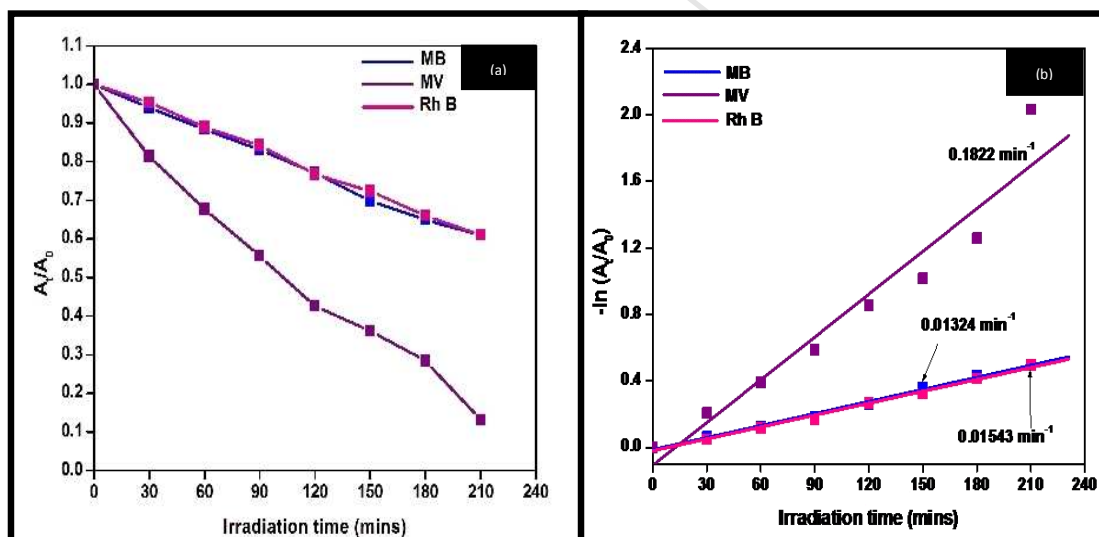
Fig. 7 Photodegradation using HNBs: (a) degradation efficiency and (b) degradation rate.

Table 1 Photocatalytic activity of HNBs

Photocatalyst	Degradation rate (min^{-1})			Degradation efficiency (%)		
	MB	**MV**	**RhB**	**MB**	**MV**	**RhB**
HNBs	0.0132	0.1822	0.0154	77.05	91.40	81.40

3.4.2. Photodegradation mechanism

The photocatalytic activity of a wide band gap photocatalyst under irradiation occurs when light with energy higher than its band gap energy creates electron–hole pairs (excitons). The photogenerated electron moves up to the conduction band whereas the hole drifts in the valence band. The photogenerated charge carriers initiate redox reactions in toxic complex dye molecules when adsorbed on the surface of the photocatalyst to degrade them. The positive-hole of the photocatalyst breaks apart a water molecule to form the hydroxyl radical ($^{\bullet}OH$) and the negative-electron reacts with an oxygen molecule to form superoxide anions ($^{\bullet}O_2^-$), hydrogen peroxide molecules (H_2O_2), hydroxyl radicals ($^{\bullet}OH$), the hydrogen dioxide anion (HO_2^-), and hydroperoxy radicals ($^{\bullet}HO_2$) [36,37]. These superoxide radicals and hydroxyl radicals then degrade the target pollutants. This photocatalytic cycle continues where the degradation efficiency depends on the nature and availability of the light source, the band gap and surface area of the photocatalyst, the structure of the dye molecules, and other factors. Photodegradation via the formation of superoxides and/or hydroxyl radicals at the HNB–dye solution interface after the production of electron–hole pairs by UV irradiation can be summarized as follows.

$$\text{HNBs} + h\nu \ (>= E_g) \rightarrow \text{HNBs} \ (e^- + h^+)$$

$$\text{HNBs} \ (e^-) + O_2 \rightarrow \text{HNBs} + {}^{\bullet}O_2^-$$

$$\text{HNBs} \ (h^+) + OH^- \rightarrow \text{HNBs} + {}^{\bullet}OH$$

$${}^{\bullet}OH/{}^{\bullet}O_2^- + (MB/MV/RhB) \rightarrow \text{Degradation products} \ (H_2O + CO_2)$$
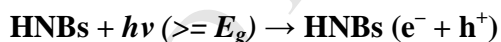
HNBs facilitate the degradation of dyes because of their intrinsically different surface reactivity (positively charged calcium-rich Ca^{2+} *c*-surface and negatively charged hydroxyl OH^- and phosphate PO_4^{3-} rich *a*-surface). When irradiated with UV light, the electron in the surface PO_4^{3-} group will become excited and create a vacancy on HAp, which is transferred to the oxygen atoms, and this is followed by the formation of $^{\bullet}O_2^-$ radicals. The superoxide radicals further react with water molecules to produce OH^- ions, which involves the oxidation of pollutants adsorbed on the surface of HAp [38]. The key factors responsible for the photocatalytic efficiency are: (i) the recombination rate of photogenerated electron–hole pairs should be slowed down by smaller particles with a reduced grain boundary density and better crystallinity; and (ii) the higher surface area facilitates the adsorption of organic molecules by increasing the number of active sites, which is favorable for the reaction kinetics. The first factor

can be satisfied by our wide band gap [39, 40] HNBs, which we confirmed based on their structural and optical properties, and the second factor was demonstrated by the BET analysis, as shown in Table 2.

Table 2 Structural, optical, and surface properties of HNBs

Crystallite Size nm	Absorption Peak nm	Band gap eV	Pore Size nm	Specific Surface Area ($m^2\,g^{-1}$)
21	257	5.1	15	31.09

The absorption peak of the HNBs at 257 nm indicates that our photocatalyst needs to be illuminated by a UV source. Moreover, the wide band gap due to the nanoscale size effect reduces the recombination rate for electron–hole pairs, thereby enhancing the degradation rate. Furthermore, the reaction mechanism indicates that the higher surface area provides more active sites, which enhances the adsorption of target molecules so more reactions can occur, and thus the photocatalytic efficiency of the HNBs is higher because both oxidation and reduction occurs on the surface of the photoexcited photocatalyst [41-43]. The results showed that the degradation of the dyes with HNBs reached up to 91%.

3.4.2.1. Effect of irradiation time

The relationship between the removal of different cationic dyes and the irradiation time using the HNB photocatalyst is shown in Fig. 6, which demonstrates the gradual decrease in the dye concentration as time increased. The concentration of the dyes in the solution was reduced to 77–91% after 210 min. In fact, the formation of superoxide radicals and hydroxyl radicals increased over time due to the higher specific surface area [44-46] of the HNBs, which facilitated the degradation of the MB, MV, and RhB molecules, thereby allowing their effective photodegradation.

3.4.2.2. Effect of cationic dyes

The photodegradation efficiency of the HNBs using different organic cationic dyes was examined for 210 min under UV radiation. Basic dyes yield positively charged ions when dissolved in water. The hydrated cations in the aqueous phase competed effectively for the adsorption sites on HNBs [47], and thus the oxidation/reduction process degraded the dyes [48].

12

The photogenerated electrons and holes could degrade most of the cationic dyes in an effective manner due to their high redox potentials [49].

4. Conclusion

In this study, HNBs were assembled from nanosticks as nanoscale building blocks via a solvothermal process without using any surfactant. The phase, crystallinity, and purity of the HNBs were structurally confirmed by XRD and FTIR. Well-formed HNBs with an average length and width of 11 and 5 µm, respectively, were characterized by FESEM. The specific surface area and pore size of the HNBs were calculated as 31.09 m^2 g^{-1} and 15 nm, respectively, by BET analysis. The optical characteristics determined by UV-Vis spectroscopy indicated the occurrence of absorption at 257 nm, with a band gap of 5.1 eV based on the Tauc plot. Furthermore, the photocatalytic activity of the synthesized HNBs was examined during the degradation of MB, MV, and RhB under UV irradiation. The effective degradation of 77–91% of various cationic dyes by the HNBs was explained in detail.

References

[1] A.L. Ahmad, W.A. Harris, Syafiie, O.B. Seng, Removal of dye from wastewater of textile industry using membrane technology, J. Tech.. 36 (2002) 31–44.

[2] I.M. Banat, P. Nigam, D. Singh, R. Marchant, Microbial decolorization of textile dye containing effluents, Biores. Tech. 58 (1996) 217–227.

[3] T. Robinson, G. Mac Mullan, R. Marchant, P. Nigam, Remediation of dyes textile effluent: a critical review on current treatment technologies with a proposed alternative, Biores. Tech. 77 (2001) 247–255.

[4] S. Sekar, M. Suriyanarayana, V. Ranganathan, D.R. MacFarlane, A.B. Mandal, Choline based ionic liquids enhanced biodegradation of azo dyes, Environ. Sci. Technol. 46 (2012) 4902–4908.

[5] R. Kumar, R. Ahmad, Biosorption of hazardous crystal violet dye from aqueous solution onto treated ginger waste (TGW), Desalination 265 (2011) 112–118.

[6] M. Doltabadi, H. Alidadi, M. Davoudi, Comparative study of cationic and anionic dye removal from aqueous solutions using sawdust-based adsorbent, Env. Prog. & Sus. Ener. 35 (2016) 1078–1090.

[7] H. Metivier-Pignon, C. Faur-Brasquet, P. Le Cloirec, Adsorption of dyes onto activated carbon cloths: approach of adsorption mechanisms and coupling of ACC with ultrafiltration to treat coloured wastewaters, Sep. Purif. Technol. 31 (2003) 03–11.

[8] S. Senthilkumaar, P.R. Varadarajan, K. Porkodi, C.V. Subbhuraam, Adsorption of methylene blue onto jute fiber carbon: kinetics and equilibrium studies, J. Coll. Int. Sci. 284 (2005) 78–82.

[9] R. Jain, M. Mathur, S. Sikarwar, A. Mittal, Removal of the hazardous dye rhodamine B through photocatalytic and adsorption treatments, J. Environ. Manag. 85 (2007) 956–964.

[10] T. Hillie, M. Munasinghe, M. Hlope, Y. Deraniyagala, Nanotechnology, water and development, Meridian Institute (2006) 1–44.

[11] K.A. Gregg, S.C. Perera, G. Lawes, S. Shinozaki, S.L. Brock, Controlled synthesis of MnP nanorods: Effect of shape anisotropy on magnetization, Chem. Mater. 18 (2006), 879–886.

[12] Z. Hai-Bin, Z. Ke-Chao, L. Zhi-You, H. Su-Ping, Z. Yan-Zhong, Morphologies of hydroxyapatite nanoparticles adjusted by organic additives in hydrothermal synthesis, J. Cent. South Univ. Technol. 16 (2009) 0871–0875.

[13] K. Ioku, S. Yamauchi, H. Fujimori, S. Goto, M. Yoshimura, Hydrothermal preparation of fibrous apatite and apatite sheet, Sol. State Ion. 151 (2002) 147–150.

[14] J. Liu, X. Ye, H. Wang, M. Zhu, B. Wang, H. Yan, The influence of pH and temperature on the morphology of hydroxyapatite synthesized by hydrothermal method, Ceram. Int. 121 (2002) 59–64.

[15] P. Sujaridworakun, F. Koh, T. Fujiwara, D. Pongkao, A. Ahniyaz, M. Yoshimura, Preparation of anatase nanocrystals deposited on hydroxyapatite by hydrothermal treatment, Mater. Sci. and Engg. C 25 (2005) 87–91.

[16] M. Yoshimura, P. Sujaridworakun, F. Koh, T. Fujiwara, D. Pongkao, A. Ahniyaz, Hydrothermal conversion of calcite crystals to hydroxyapatite, Mater. Sci. and Engg. C 24 (2004) 521–525.

[17] S.B. Chen, Y.B. Ma, L. Chen, K. Xian, Adsorption of aqueous Cd^{2+}, Pb^{2+}, Cu^{2+} ions by nano-hydroxyapatite: Single- and multi-metal competitive adsorption study, Geochem. J. 44 (2010) 233–239.

[18] H. Nishikawa, K. Omamiuda, Photocatalytic activity of hydroxyapatite for methyl mercaptane, J. Mol. Catal. A: Chem. 179 (2002) 193–200.

[19] J.H. Shariffuddin, M.I. Jones, D.A. Patterson, Greener photocatalysts: Hydroxyapatite derived from waste mussel shells for the photocatalytic degradation of a model azo dye wastewater, Chem. Eng. Res. and Des. 91 (2013) 1693–1704.

[20] H. Nishikawa. A high active type of hydroxyapatite for photocatalytic decomposition of dimethyl sulfide under UV irradiation, J. Mol. Catal. A: Chem. 207 (2004) 149–153.

[21] R.A. Ramli, R. Adnan, M.A. Bakar, S.M. Masudi, Synthesis and characterisation of pure nanoporous hydroxyapatite, J. Phy. Sci. 22 (2011) 25–37.

[22] G.A. Martinez-Castanon, J.P. Loyola-Rodriguez, N.V. Zavala-Alonso, Preparation and characterization of nanostructured powders of hydroxyapatite, Superficies y Vacio 25 (2012) 101–105.

[23] A. Balamurugan, J. Michel, J. Faure, et al., Synthesis and structural analysis of sol gel derived stoichiometric monophasic hydroxyapatite, Cer. Silikaty, 50 (2006) 27–31.

[24] Y.J. Wang, J.D. Chen, K. Wei, S.H. Zhang, X.D. Wang, Surfactant-assisted synthesis of hydroxyapatite particles, Mater. Lett. 60 (2006) 3227–3231.

[25] A. Rapacz-Kmita, A. Slosarczyk, Z. Paszkiewicz, C. Paluszkiewicz, Phase stability of hydroxyapatite-zirconia ($HAp-ZrO_2$) composites for bone replacement, J. Mol. Struct. 704 (2004) 333–340.

[26] F. Manoli, E. Dalas, Spontaneous precipitation of calcium carbonate in the presence of ethanol, isopropanol and diethylene glycol, J. Cryst. Growth 218 (2000) 359–364.

[27] X.W. Lou, Y. Wang, C.L. Yuan, J.Y. Lee, L.A. Archer, Template-free synthesis of SnO_2 hollow nanostructures with high lithium storage capacity, Adv. Mater. 18 (2006) 2325–2329.

[28] H. Alobeedallah, J.L. Ellis, R. Rohanizadeh, H. Coster, F. Dehghani, Preparation of nanostructured hydroxyapatite in organic solvent for clinical applications, Trends Biomater. Artif. Organs 25 (2011) 12–19.

[29] I. Reeta Mary, S. Sonia, S. Viji, D. Mangalaraj, C. Viswanathan, N. Ponpandian, Novel multiform morphologies of hydroxyapatite: Synthesis and growth mechanism, Appl. Surf. Sci. 361 (2016) 25–32.

[30] A. Kolodziejczak-Radzimska, M. Samuel, D. Paukszta, A. Piasecki, T. Jesionowski, Synthesis of hydroxyapatite in the presence of anionic surfactant, Physicochem. Probl Miner. Process 50 (2014) 225–236.

[31] S. Lowell, Introduction to Powder Surface Area, John Wiley and Sons, 1979.

[32] R. Murugan, S. Ramakrishna, Production of ultra-fine bioresorbable carbonated hydroxyapatite, Acta Biomater. 2 (2006) 201–206.

[33] K. Lin, L. Xia, J. Gan, Z. Zhang, H. Chen, X. Jiang, J. Chang, Tailoring the nanostructured surfaces of hydroxyapatite bioceramics to promote protein adsorption, osteoblast growth, and osteogenic differentiation, ACS Appl. Mater. Inter. 5 (2013) 8008–8017.

[34] K. Matsunaga, A. Kuwabara, First-principles study of vacancy formation in hydroxyapatite, Phys. Rev. B, 75 (2007) 1–9.

[35] Ines S. Neira, Yury V. Kolenko, Oleg I. Lebedev, et al., An effective morphology control of hydroxyapatite crystals via hydrothermal synthesis, Cryst. Growth Des. 9 (2009) 466–474.

[36] S. Baruah, J. Dutta, Nanotechnology applications in pollution sensing and degradation in agriculture: a review, Environ. Chem. Lett. 7 (2009) 191–204.

[37] S. Banerjee, J. Gopal, P. Muraleedharan, A.K. Tyagi, B. Raj, Physics and chemistry of photocatalytic titanium dioxide: visualization of bactericidal activity using atomic force microscopy, Curr. Sci. 90 (2006) 1378–1383.

[38] M.P. Reddy, A. Venugopal, M. Subrahmanyam, Hydroxyapatite photocatalytic degradation of calmagite (an azo dye) in aqueous suspension, Appl. Cat. B: Env. 69 (2007) 164–170.

[39] S. Senthilkumaar, K. Porkodi, Heterogeneous photocatalytic decomposition of Crystal Violet in UV-illuminated sol-gel derived nanocrystalline TiO2 suspensions, J. Coll. Int. Sci. 288 (2005) 184–189.

[40] C. Sahoo, A.K. Gupta, A. Pal, Photocatalytic degradation of Crystal Violet (Ci Basic Violet 3) on silver ion doped TiO_2, Dyes and Pig. 66 (2005) 189–196.

[41] C.H. Cho, D.K. Kim, D.H. Kim, Photocatalytic activity of monodispersed spherical TiO$_2$ particles with different crystallization routes, J. Am. Chem. Soc. B6 (2003) 1138–1145.

[42] Y. Oguri, R. Riman, H.K. Bowen, Processing of anatase prepared from hydrothermally treated alkoxy derived hydrous titania, J. Mater. Sci. 90 (1988) 2897–2904.

[43] J.L. Look, C.F. Zukoski, Shear induced aggregation during precipitation of titanium alkoxide, J. Colloid Interface Sci. 153 (1992) 461–482.

[44] E.S. Elmolla, M.Chaudhuri M, Degradation of amoxicillin, ampicillin and cloxacillin antibiotics in aqueous solution by the UV/ZnO photocatalytic process, J. Hazard Mater.173 (2010) 445–449.

[45] K. Hayat, M. Gondal, M.M. Khaled, S. Ahmed, A.M. Shemsi, Nano ZnO synthesis by modified sol gel method and its application in heterogeneous photocatalytic removal of phenol from water, Appl. Catal. A 393 (2011) 122–129

[46] C. Tian, Q. Zhang, A. Wu, M. Jiang, Z. Liang, B. Jiang, H. Fu, Cost-effective large-scale synthesis of ZnO photocatalyst with excellent performance for dye photodegradation, Chem. Commun. 48 (2012) 2858–2860.

[47] B. Ali Fil, C. Ozmetin, M. Korkmaz, Cationic dye (methylene blue) removal from aqueous solution by montmorillonite, Bull. Korean Chem. Soc. 33 (2012) 3184–3190.

[48] T. Pizzolato, Colour removal with NaClO of dye wastewater from an agate-processing plant in Rio Grande do Sul, Brazil, Int. J. Min. Pro. 65 (2002) 3–4.

[49] U.I. Gaya, A.H. Abdullah, Heterogeneous photocatalytic degradation of organic contaminants over titanium dioxide: A review of fundamentals, progress and problems, J. Photochem. Photobiol. C 9 (2008) 01–12.

Highlights

- Hydroxyapatite nested bundles (HNBs) constructed via a solvothermal method.

- Structural, surface, and optical properties characterized

- HNBs effectively photocatalyzed the degradation of dyes under UV irradiation.